Vrije Universiteit Brussel

**VRIJE
UNIVERSITEIT
BRUSSEL**

EIS comparative study and critical Equivalent Electrical Circuit (EEC) analysis of the native oxide layer of additive manufactured and wrought 316L stainless steel

Revilla, Reynier I.; Wouters, Benny; Andreatta, Francesco; Lanzutti, Alex; Fedrizzi, Lorenzo; De Graeve, Iris

EIS comparative study and critical Equivalent Electrical Circuit (EEC) analysis of the native oxide layer of additive manufactured and wrought 316L stainless steel

Reynier I. Revilla[1,*], Benny Wouters[1], Francesco Andreatta[2], Alex Lanzutti[2], Lorenzo Fedrizzi[2], Iris De Graeve[1]

[1]*Vrije Universiteit Brussel (VUB), Department of Chemistry and Materials, Research Group of Electrochemical and Surface Engineering (SURF), Pleinlaan 2, 1050 Brussels, Belgium*

[2]*Polytechnic Department of Engineering and Architecture, University of Udine, Via del Cotonificio, 108-33100 Udine, Italy*

*Corresponding author. E-mail address: rrevilla@vub.be (R. I. Revilla)

Abstract:
In this work, a comparative electrochemical impedance spectroscopy (EIS) study of the native oxide layer of selective laser melted and wrought 316L stainless steel is conducted. A careful examination of the data is carried out in order to properly identify the appropriate model to fit the EIS response. From the parameters calculated by fitting the EIS data and a complementary XPS analysis, the electrical and dielectric characteristics of the passive oxide layers of the specimens were obtained. Clear differences were noticed between the two materials, which could definitely contribute to the overall understanding of the corrosion behavior of these materials.

Keywords:
Additive manufacturing; 316L stainless steel; Electrochemical Impedance Spectroscopy

Introduction

Austenitic stainless steels (SS) are widely known for their numerous industrial applications. Due to their relatively high chromium content, which enables the formation of a Cr_2O_3–based passive layer, austenitic stainless steels present a good corrosion resistance [1,2]. However, despite their name, stainless steels can still be susceptible to pitting corrosion in highly corrosive media [3]. Their corrosion resistance is highly dependent on the phases present, which are related to the specific alloying elements added. After the 304 SS (Fe-Cr-Ni), the second most used austenitic steel is the 316 SS (Fe-Cr-Ni-Mo). Their main difference consists of an addition of Mo (2 – 3 %) to the 316 SS. This Mo added is known to increase their resistance against corrosion [4–7]. 316L grade is the low carbon version of the 316 stainless steel.

Austenitic SS are usually prepared by casting or in wrought form. However, in recent years, metal additive manufacturing (MAM) has arisen as a very promising technique to manufacture dense and geometrically complex SS components [8,9]. Among the various MAM processes, selective laser melting (SLM) is one of the most used techniques. During SLM, a laser source selectively scans and melts over a metal powder bed, building complex parts in a layer–by–layer fashion [8-13]. The special conditions associated with the MAM processes (e.g. extremely fast cooling rates) promote the formation of very fine microstructure and distribution of alloying elements [8-13]. The microstructure of additive manufactured (AM) 316L SS is characterized by very fine interconnected cellular or columnar sub-grains (with a size between 0.5 μm and 1 μm) that are confined within larger single-crystal grains with size in the range of 10 – 100 μm [14-19]. Previous works have found that the sub-grain boundaries are enriched with Mo [14-17,20,21], and some of those works reported not only an enrichment of Mo but also of Cr at the borders of the sub-grains [16,17,21]. Furthermore, austenite has been the main crystalline phase found in AM 316L SS [15]. However, small traces of δ-ferrite have also been reported in previous studies [14,16].

The unique manufacturing conditions from MAM are known to greatly influence not only the microstructure but also the corrosion behavior of 316L SS. Several works have been dedicated to this topic in recent years [16-20,22-28]. Nevertheless, the results are somewhat inconclusive. A table summarizing the most relevant studies carried out to date concerning the corrosion behavior of AM 316L SS compared with conventionally manufactured specimens can be seen in the appendix. A number of works have reported an increased pitting resistance for SLM 316L specimens compared to as-cast [22] and wrought samples [17-19,23-25]. All of these studies reported similar values of corrosion potential for SLM and classically manufactured 316L SS, however, a much wider passive window was always found for the SLM 316L samples compared to the as-cast/wrought specimens [17-19,22-25]. On the other hand, other researchers have reported a poorer corrosion resistance and increased corrosion current densities for SLM 316L samples compared to wrought material [26,27]. Moreover, 316L SS samples fabricated using other MAM processes have been shown to exhibit lower resistance against corrosion than that of wrought 316L SS [16,20,28]. In all those cases, the reduced corrosion resistance was explained to be the result of the existence of heterogeneities, small amounts of δ-ferrite, and micro-segregation effects inherent from the MAM processes. Nevertheless, it is important to notice that the anodic polarization data shown in some of the studies claiming inferior corrosion resistance for AM 316L SS compared to wrought 316L SS [20,27] do not look like typical polarization responses, being

possibly influenced by crevice corrosion. Additionally, in other cases the low corrosion resistance of the AM 316L specimens could have been the result of a remarkably high level of porosity [26]. Concerning the works reporting a superior corrosion resistance of SLM 316L samples compared to wrought material, two main ideas have been proposed/used to explain this observation. Q. Chao et al. [23] concluded that the high solidification rates inherent to additive manufacturing avoided MnS formation and an associated Cr-depletion zone, which minimizes initiation sites for localized corrosion. S.H. Sun et al. [24] and G. Sander et al [25] also suggested (with no direct proof) that the SLM process may impact the formation of inclusions, in a way that the inclusions are either annihilated or are too small to promote pit initiation in SLM 316L. Alternatively, other researchers suggested that the higher corrosion resistance exhibited by SLM 316L SS samples compared to the wrought material is the result of better barrier properties of the native oxide film [17-19]. Nevertheless, they all concluded that the thickness and the composition of the oxide film on SLM 316L specimens are very similar to that of the oxide on wrought SS [17-19]. Therefore, a more detailed and in-depth characterization of the native oxide layer formed on SLM and wrought 316L SS could definitely contribute to the overall understanding of the corrosion behavior of these materials.

Electrochemical impedance spectroscopy (EIS) has been extensively used for the characterization of oxide layers on the surface of metals and alloys [29-36]. The main purpose of EIS in those cases is to determine the oxide film capacitance, which is subsequently used to estimate the thickness and/or dielectric properties of the insulating layer. Through an EIS analysis, the barrier properties of the insulating layer can be assessed. Nevertheless, a reliable characterization of the native oxide film properties by EIS relies on a correct choice of the equivalent electrical circuit (EEC) used to fit the experimental data. M.J.K. Lodhi et al. [18,19] used EIS as a complementary technique to demonstrate the better barrier characteristics of the SLM 316L SS relative to the wrought material. Besides the ohmic resistance associated with the electrolyte, their EEC consisted of a constant-phase element (CPE) and a parallel resistance. They used the values of the parallel resistance and the CPE parameter (Q) to evaluate the barrier properties of the native oxide layer. However, as reported by M.E. Orazem et al. [29], the parameter Q does not represent the true capacitance of the oxide layer, and the parallel resistance may be attributed not only to reactions taking place at the electrolyte/metal interface, but also to interconnecting conductive phases within the solid matrix.

In this work, a comparative EIS study of the native oxide layer of SLM and wrought 316L is conducted. A careful examination of the data is carried out in order to properly identify the appropriate model from which the properties of the oxide film can be acquired. An XPS analysis was also conducted. From the results of the XPS study and the parameters calculated by fitting the EIS response, the electrical and dielectric characteristics of the passive oxide layers of the specimens was obtained. Clear differences were noticed between the two materials.

Experimental section

Samples
The SLM 316L specimens were prepared using a Concept Laser M2 Cusing machine, equipped with a 400 W laser in an argon atmosphere with resulting oxygen content of < 0.2 %. The chemical

composition of the commercial 316L stainless steel powder used for the production of the samples is shown in Table 1. Rectangular cuboids with the size of 30.5×20.5×7 mm were produced with the major surface parallel (SLM-XY samples) and perpendicular (SLM-XZ samples) to the building platform. A laser power of 180 W, 600 mm/s scanning speed, 25 μm layer thickness, 30% hatch distance, and a spot diameter of 120 μm were used for the fabrication of the samples, resulting in a laser energy density of 300 J/mm^3. The same scanning strategy as the one described in reference [17] was used for the fabrication of the samples. No post heat treatment was applied on the SLM specimens. Additionally, a commercial wrought 316L SS with approximately the same chemical composition was used as a comparison. The chemical composition of the samples is the same as that shown in reference [17]. All the samples were mechanically ground and polished to a 1 μm surface finishing.

Experimental techniques
The optical characterization of the samples was conducted using a Leitz Metallovert optical microscope. Morphology and microstructure characterization was carried out by means of scanning electron microscopy. An FE–SEM JEOL JSM–7100F with 15 kV acceleration voltage, 5 nA probe current, and a working distance of 10 mm was used. To highlight the microstructural features, the samples were etched in Vilella's reagent (5 ml HCl, 1 g picric acid, and 100 ml 95% ethanol).

The XPS measurements were conducted using a PHI-5600ci XPS spectrometer (Physical Electronics) with the hemispherical analyzer detector at 90° with respect to the surface of the sample. A diameter aperture of 800 μm was used. The X-ray source was operating at 100 W with a bias voltage of 14.5 kV.

Potentiodynamic polarization experiments were carried out using an Elektroniklabor Peter Schrems Potentiostat with a current resolution in the order of 10 fA. A three–electrode cell configuration consisting of the sample as working electrode, a Pt counter electrode, and an Ag/AgCl (3 M KCl) reference electrode was used. The measurements were carried out in an Avesta cell to avoid crevice corrosion during potentiodynamic polarization. The electrolyte used was a 3.5 wt% NaCl solution at room temperature. The potentiodynamic test was conducted 15 min after immersion in the electrolyte in order to wait for the system to stabilize. The scans were performed in the anodic direction at a rate of 0.2 mV/s. For each sample, at least 3 potentiodynamic polarization curves were obtained.

Electrochemical impedance spectroscopy (EIS) was performed in 3.5 wt% NaCl using a Bio-Logic VMP3 potentiostat. The frequency range applied was 200 kHz to 10 mHz and the signal amplitude used was V_{rms} = 15 mV. 10 measurement points were obtained per frequency decade. The experimental EIS setup was placed in a Faraday cage in order to reduce the influence of external noises. The EIS measurements were conducted after 1 h of immersion in the electrolyte. Two to three consecutive EIS measurements were executed in order to confirm the stability of the system. A three–electrode cell configuration consisting of the sample as working electrode, a platinum counter electrode, and a saturated Ag/AgCl (210 ± 15 mV vs SHE) reference electrode was used for the experiments. A circular section with a diameter of 1 cm was the area of the samples exposed to the electrolyte during the measurements. Each measurement was repeated from 3 to 6 times for each sample.

Results and discussion

Initial microstructure characterization

Figure 1 presents optical images of the etched surface of the wrought and the SLM 316L SS samples. As can be seen in Figure 1a, the wrought sample exhibits typical polygonal shape coarse austenitic grains. On the other hand, in the optical images of the SLM specimens (Figure 1b and 1c), the laser tracks from the MAM process can be easily distinguished. On the surface parallel to the building platform (XY) overlapping elongated tracks can be seen (see Figure 1b), while a scale-like pattern can be identified on the surface perpendicular (XZ) to the building platform (see Figure 1c). The borders of the melt pools are easily recognized after metallographic etching.

At the micro-scale, a dense network of sub-grains with an etch-resistant border can be seen on the surface of the SLM samples with the use of scanning electron microscopy (see inset in Figure 1c). These cells have a width of around 1 μm. Large colonies of round and elongated cells coexisting on the surfaces of the SLM 316L specimens can be easily seen regardless of the plane analyzed. The same microstructure has been described elsewhere [14-19]. Hence, the number of images showing this microstructure was limited.

Moreover, the porosity of the SLM samples was found to be very low and with a small pore size. As in reference [17] (in which the same SLM parameters were used), the porosity of the SLM specimens was in the order of $0.1\% - 0.2\%$. Therefore, the electrochemical behavior is not affected by the porosity in these samples [25]. Additionally, no inclusions could be detected in the SLM specimens. This has also been reported by other researchers [15,17,23,25,27].

Native oxide layer characterization by XPS

From the XPS analysis, Fe, Cr, Ni, and Mo were identified. XPS survey spectra of the wrought and SLM 316L SS samples are shown in Figure 2. As can be seen in the figure, the XPS spectra of the polished samples were almost identical, which demonstrate no change in the surface chemistry of the specimens. Only the spectrum taken in one of the surfaces of the SLM sample is shown since they were all very similar. Both oxidized and metallic states of Fe and Cr could be detected. As shown in other works, due to the high content of Cr in this type of alloy, the thickness of the native oxide layer (*d*) can be estimated considering the intensity of the Cr peaks originating from the oxide and metal substrate [37]. Other researchers have used Equation (1) to calculate the passive film thickness [37].

$$d = \lambda \ln[1 + I_{Cr,ox}/I_{Cr,met}] \tag{1}$$

Where λ is the medium free path length for photoelectrons from Cr, for which a value of 1.7 nm is commonly used [37]. $I_{Cr,ox}$ and $I_{Cr,met}$ are the oxide and metal contribution of the Cr peaks respectively. To calculate the thicknesses using Equation (1) only the $Cr2p_{3/2}$ component was fit due to the known overlap of a satellite feature of the $Cr2p_{3/2}$ peak on the $Cr2p_{1/2}$ component in Cr(III) oxide [38,39]. The deconvolution of the $Cr2p_{3/2}$ component was carried out using a multiplet for the oxide contribution and an asymmetric peak for the metal contribution. Figure 3a shows high-resolution XPS spectra of the Cr2p region for the wrought and SLM 316L SS samples. There is an almost complete overlap between the spectra. The same was seen for all the other elements, which further confirms no compositional difference between the native oxide layer of

the wrought and that of the SLM sample. As a reference, the high-resolution spectra of the O1s region for the wrought and SLM samples is also shown in Figure 3b. A main contribution from the metal oxides can be clearly seen at around 530 eV, while an additional contribution can be seen at around 531.5 eV. This second contribution could be due to the presence of metal hydroxides, which can also slightly overlap with organic contamination (C=O can be usually seen in the region 531.5 – 532 eV). Nevertheless, it is important to notice that there is an almost complete overlap between both spectra, which demonstrates that the composition of these native oxides is the same.

The calculated thickness of the passive oxide layer of the wrought, the SLM_XY, and the SLM_XZ surface was 3.9, 3.8, and 4 nm respectively. These values are in agreement with thicknesses obtained in previous works [29,37,40]. As can be noted, all the samples present approximately the same value of passive oxide layer thickness. This is in accordance with what was suggested by F. Andreatta et al. from the characterization carried out using GDOES [17].

Potentiodynamic polarization curves

Figure 4 shows potentiodynamic polarization curves for wrought and SLM 316L SS. Since the same behavior was obtained for the XY and the XZ surface of the SLM sample, only one curve is used for the SLM material. The corrosion potential of wrought and SLM specimens was very similar. This value ranged from -0.1 to -0.2 V vs Ag/AgCl (3M KCl) for both samples. This is in agreement with results presented in a previous study [17]. However, slightly lower passivity currents and a much wider passive window can be easily identified for the SLM 316L sample compared to the wrought specimen, indicating an increased pitting resistance for SLM 316L in comparison with the wrought material. This is perfectly in line with previous works [17-19,23-25]. The enlarged passivity of the SLM specimen compared to the wrought sample could be the result of a more stable native oxide film.

EIS results

In order to gain insights regarding the barrier properties of the native oxide layer of the specimens, EIS measurements were conducted. The typical Bode plots obtained from the different samples are shown in Figure 5. The electrochemical impedance measured at relatively high frequencies (from 10^4 to 10^5 Hz in this case – see Figure 5a) is generally related to the resistance of the electrolyte [41], which, as can be seen in Figure 5a, remains constant during the measurements. In the middle range and low frequencies (from 10^3 to 10^{-2} Hz – see Figure 5a and 5b) a clear capacitive behavior can be observed from the Bode diagram. This is associated with the native oxide layer on the surface of the specimens. Additionally, a single time constant, related also to the oxide layer, can be identified from the phase angle (Figure 5b). The phase angle for all samples mostly overlaps. However, a slight difference can still be noticed between the SLM specimens and the wrought material, especially in the impedance modulus. The middle range and low frequency signal of the wrought sample was consistently slightly lower than the impedance signal of the SLM materials. On the other hand, the impedance signal of the SLM samples was approximately the same independently of the surface analyzed (XY or XZ). More details can be seen in Figure 5c, which shows a zoom of the impedance plot in the frequency range from 1 to 10^{-2} Hz. Additionally, the average values of the impedance measured at the lowest frequency (10^{-2} Hz) are plotted in

Figure 6. Even though, a relatively large standard deviation was obtained for the XZ surface of the SLM material, a slight shift towards higher impedance values is seen for the SLM samples compared to the wrought specimen. The impedance value at the lowest frequency provides an indication of the barrier properties of the oxide layer. This is in good agreement with the anodic polarization experiments, in which slightly lower passivity currents and a much wider passive region were observed for the SLM specimen compared to the wrought material (see Figure 4).

Fitting and analysis of the EIS response
To determine the oxide film capacitance from the EIS data, several equivalent electrical circuits (EEC) have been employed in literature [29-34]. The main EECs used are shown in Figure 7. In the circuit represented in Figure 7a the oxide layer is considered as a capacitor, while in the circuits of Figure 7b and 7c a CPE and a Young element (Z_Y) are considered respectively. In this work, all the EIS data obtained were fitted using the three equivalent electrical circuits represented in Figure 7. The origin of a CPE has been attributed to the distribution of time constants along or normal to the electrode surface. In the case of a distribution along the electrode surface, the model developed by Brug et al. [42] can satisfactorily describe the impedance response. On the other hand, several models have been proposed to characterize the impedance associated with the distribution of time constants normal to the electrode surface [29]. Two particular models describing resistivity distributions normal to the electrode surface are the power-law model [43,44] and the Young model [30,45,46]. The power-law model delineates a power-law distribution of resistivity within the oxide layer, and correlates CPE parameters with film properties. On the other hand, the Young model assumes an exponential variation of resistivity through the oxide layer.
In order to identify the normal resistivity distribution that best describes the oxide layer of our samples, the methodology presented by Y.M. Chen et al. [47] was employed. This method is based on the Voigt fitting model. In this approach, dimensionless resistivity (ρ/ρ_δ) is plotted as a function of dimensionless position (ξ). If the sample is characterized by a power-law distribution of resistivity, a linear relationship should be found in a log-log scale. On the other hand, if the sample is characterized by an exponential variation of resistivity (distinctive of the Young model) a linear relationship can be found in a semi-logarithmic scale. All the EIS data measured in this study were analyzed using this methodology. No linear relation was found between resistivity and position in a log-log representation. However, a linear behavior was observed for the data plotted in a semi-logarithmic scale. This can be clearly seen in Figure 8, in which an example from EIS data obtained in the SLM_XY specimen is shown. Therefore, the Young model was assumed to be the best model describing the EIS data, and hence the main model considered in this work. Nevertheless, the EECs represented in Figure 7a and 7b were also used for comparison purposes.
Equations (2) and (3) represent the impedance of a CPE and a Young element respectively.

$$Z_{CPE} = \frac{1}{Q(j\omega)^\alpha} \tag{2}$$

$$Z_Y = \frac{p}{j\omega C_Y} ln \left[\frac{1+j\omega\tau \cdot \exp\left(p^{-1}\right)}{1+j\omega\tau} \right] \tag{3}$$

Where j is the imaginary unit ($j^2 = -1$) and ω the angular frequency. Q and α ($0 \leq \alpha \leq 1$) are the parameters associated with the CPE, while p (relative penetration depth), τ (time constant), and C_Y (oxide film capacitance) are the parameters of the Young element.

In general, a good fitting of the experimental data was achieved by using a CPE or a Young element to describe the native oxide layer. By using a capacitor (EEC represented in Figure 7a), relatively larger errors were obtained. Figure 9 shows an example of a fitted electrochemical impedance data using a Young element. In such a case, a maximum residual of 6 % was obtained for the impedance modulus, while by using a CPE, residuals up to 9.2 % were acquired. This demonstrate a better fitting of the data using a Young element (EEC shown in Figure 7c) than using a CPE (EEC shown in Figure 7b).

As mentioned above, from each sample type, 3 to 6 EIS signals were fitted. Per model used, an average value of each parameter is then calculated for every type of sample. Table 2 shows the average values and standard deviation of the different parameters obtained per sample type from the fitting of the data using the EECs shown in Figure 7.

By using the Young model, the capacitance of the film is directly obtained through parameter C_Y. The average value of this parameter per sample is represented in Figure 10a. Very similar values for the capacitance of the oxide layer of the XY and the XZ surface of the additive manufactured sample are obtained. However, a clear difference can be observed between the capacitance of the oxide layer of the SLM specimen and the wrought sample. The capacitance of the wrought sample is about 1.8 times higher than that of the SLM sample. The capacitance is related to the thickness (*d*) and the dielectric constant (ε) through the expression:

$$C = \frac{\varepsilon \varepsilon_0 A}{d} \tag{4}$$

Where ε_0 is the permittivity of vacuum (ε_0 = 8.8542E–14 F/cm) and *A* is the surface area.

By using the thickness of the oxide films calculated by XPS (see section above), and assuming that the active surface area for all the samples is equal to the geometric area exposed (0.7854 cm^2), the dielectric constant of the native oxide layers can be calculated. Figure 10b portrays the values of ε obtained for each specimen (45.7, 25, and 27 for the wrought, the SLM-XY, and the SLM-XZ sample respectively). The values of dielectric constant obtained for the SLM samples are close (only slightly higher) to those used in previous studies for the same material (from 12 to 25) [29,48-51]. However, the value obtained for the wrought sample differs from those often used in literature. The relatively high values of dielectric constant calculated in this work could also be due to an overestimation of the oxide film thickness caused by the presence of a contamination overlayer. Nevertheless, the almost complete overlap between the XPS spectra (see Figures 2 and 3) demonstrates that this contamination layer would have a similar contribution for all the samples. Additionally, a notable difference is observed between the wrought and the SLM material. Moreover, the value of the magnitude *d*/ε for each sample is represented in Figure 10c. Several studies have proposed *d*/ε as a measure of the effective dielectric thickness for thin layers (d < 50 nm) [52,53].

In order to verify the difference obtained between the dielectric constant of the wrought sample and the SLM specimen, the methodology described by Revilla et al. [54] was conducted. This procedure employs force spectroscopy mode of atomic force microscopy (AFM). By using this method, the relation between the dielectric susceptibilities ($\chi = \varepsilon - 1$) of the samples could be estimated at different AFM probe-sample separations. Even though this method is mostly applicable to thicker oxide layers with relatively low values of dielectric constant ($\varepsilon < 10$), it could give an indication of the relation between the two materials. Not much details concerning the calculations done with this methodology are given in this work since it is not the main focus of

this study. This approach has been well described in previous works [54,55]. The result obtained is shown in Figure 11. The value of the ratio between the dielectric susceptibilities of the samples obtained at the highest count frequency is around 1.36. This value differs lightly from that calculated using the dielectric constants obtained in this work by EIS (~ 1.8). However, the reason for this difference could be due to the fact that the thickness and dielectric constant of these native oxide layers are outside of the ideal applicability range of this methodology. Nevertheless, these results indicate that the dielectric permittivity of the native oxide layer of the wrought sample seem to be higher than that of the SLM specimen, which corresponds with what was obtained using the EIS results.

In general, the clear differences observed in the capacitance and dielectric properties between the wrought sample and the SLM specimen could be the result of structural and/or compositional differences in their native oxide layer. As suggested by other researchers [23,25], the high solidification rates inherent to the additive manufacturing process could have an impact on the size and density of the inclusions formed in the material. Consequently, this could affect the structure of the formed native oxide. Moreover, clear differences in the microstructure of the wrought and SLM specimens were observed. The SLM samples presented a cellular structure with thin and etch-resistant intercellular walls that form a three-dimensional network. As shown by other researchers, this etch-resistant network exhibit slightly different chemical composition compared to the material within the cells [14-17,20,21]. The walls of the cells seem to present a slightly higher amount of Mo (and possibly also Cr) [14-17,20,21]. As demonstrated by Pardo et al. [6], Mo added to 304 and 316 SS can modify the passive film rendering it more stable against breakdown caused by the attack of aggressive Cl^- ions. Therefore, the unique microstructure resulting from the special conditions of the SLM process could influence the structure of the native oxide layer. Additionally, in general, other factors such as density of grain boundaries and number of defects, could also affect the barrier properties of the oxide film.

In Table 2 can also be noted that, despite the high standard deviation, the average value of the parallel resistance (Rp) calculated for the SLM samples was always higher than that of the wrought material. Figure 12 shows the box plots of the parallel resistance obtained using the EEC represented in Figure 7c (Young model) for the wrought and the SLM 316L specimens. This parallel resistance can be attributed to reactions taking place at the electrolyte/metal interface, or to interconnecting conductive phases within the solid matrix. If Rp is associated with the polarization resistance of the samples, this would indicate better barrier properties for the SLM specimen in relation with the wrought sample. This agrees with the slightly lower passivity current observed for the SLM sample compared to the wrought material in the anodic polarization experiments.

Moreover, a closer look at the parameters obtained by using the Young model reveals that the relative penetration depth (p) was almost the same for all the samples (see Table 2). This parameter is only related to a characteristic length (δ) and the thickness of the oxide layer (p = δ/d [30]). Therefore, this is in agreement with the XPS results and confirms that the oxide thickness is approximately the same for all the samples. On the other hand, the calculated time constant (τ) of the wrought sample and the SLM specimen differed 3 orders of magnitude (~ 10^{-7} for the wrought specimen, and ~ 10^{-10} for the SLM samples). τ is directly proportional to the dielectric constant of the passive layer and inversely proportional to the oxide conductivity at the metal/oxide interface

(σ_0), ($\tau = \varepsilon\varepsilon_0/\sigma_0$ [30]). Therefore, not only is the dielectric constant different, but the conductivity of the oxide layers at the metal/oxide interface for the wrought and the SLM sample differ by 2 to 3 orders of magnitude. By using the values of the characteristic length (δ) and the conductivity at the metal/oxide interface (σ_0) from the fitting of the Young model, the conductivity profiles of the oxide films can be obtained. Figure 13a represents the mean conductivity profiles obtained for the wrought and the SLM samples in a semi-logarithmic scale. A large divergence can be seen at the interface between the oxide layer and the metal matrix. However, the conductivity profiles tend to converge at the surface of the oxide layer. It is important to notice that there is a significant difference between the scale of the y-axis of Figure 13b and that of Figure 13c. These distinct differences in the conductivity profiles could be the result of structural differences between the passive films of the wrought and the SLM material, especially at the metal/oxide interface.

The higher values of the conductivity at the metal/oxide interface for the SLM specimen compared to the wrought sample can be associated with a lower electrical resistivity. This might seem contradicting the fact that SLM specimens presented slightly higher values of Rp (see Figure 12) and a higher resistance against corrosion. However, establishing a direct link between the electrical resistivity of the native oxide layer and charge transfer processes is not a straightforward issue. The charge transfer resistance is related to a kinetically-controlled electrochemical reaction. In the case of a metal substrate in contact with an electrolyte, the metal molecules can electrolytically dissolve into the electrolyte (see Equation 5).

$$M \leftrightarrow M^{n+} + ne^- \tag{5}$$

During the charge transfer, not only electrons enter the metal, but also metal ions diffuse into the electrolyte. The speed at which this charge transfer reaction occurs depends on the kind of reaction, the temperature, the concentration of the reaction products, and the potential. However, the electrical resistivity of the native oxide film depends mainly, besides the temperature, on the metal itself and the molecular structure of this oxide. The electrical resistivity of the native oxide is independent of the kind of reaction taking place at the metal-electrolyte interface. Therefore, even though a lower electrical resistivity at the metal/oxide interface was calculated for the SLM 316L samples compared with the wrought specimen, this does not mean that the SLM samples would present a lower charge transfer resistance.

As demonstrated by XPS, the thickness and chemical composition of the oxide layer is almost the same for wrought and SLM material. Therefore, the passivity breakdown in this case could be associated with the existence of defects in the passive oxide layer or with structural differences in the oxide film, influencing its protective behavior. The high solidification rates intrinsic of MAM seem to affect the microstructure and distribution of alloying elements in this material. This is clearly seen in the fine, Mo- and Cr-rich, etch-resistant, and three-dimensional network formed in the SLM specimens (see inset of Figure 1c) [14-17,20,21]. This fine and unique distribution of alloying elements could influence the structure and stability of the native oxide layer, and consequently the corrosion behavior of this material. A more detailed and high resolution characterization of the native oxide film of SLM and wrought 316L SS could definitely contribute to a better understanding of the effect of microstructure on the naturally formed passive layer on the surface of these materials.

Ultimately, the authors highly recommend the use of EIS in experimental setups in which AM 316L SS has shown poorer corrosion performance than its wrought counterpart. The EIS response could help to identify the nature of each phenomenon taking place at the surface of the material, since each of them is characterized by a specific time constant. For instance, the role of porosity for highly porous specimens in a corrosive medium might be distinguishable in EIS spectra. This could, therefore, assist in defining the role that each factor plays in the corrosion process. In this work, a single time constant was identified for all the samples (see Figure 5b), which was associated with the effect of the native oxide layer. Therefore, other factors such as for instance porosity, do not seem to play a major role in the corrosion process.

Conclusions

1) SLM 316L stainless steel presented similar corrosion potential as that of the wrought specimen in 3.5 wt% NaCl. However, a much higher pitting resistance characterized the SLM samples compared to the wrought material.

2) From the XPS analysis was concluded that there is almost no difference in the thickness and surface chemistry of the native oxide film of the wrought and SLM 316L stainless steel.

3) Electrochemical impedance spectroscopy showed to be a very sensitive and powerful tool to characterize the native oxide layer of the SLM and wrought 316L stainless steel samples. The EIS analysis revealed that:

   - No difference was found in the electrochemical response of the two different planes of the SLM specimens (XY and XZ).

   - The Young impedance proved to be the most appropriate model to fit the electrochemical response associated with the native oxide layer of the materials analyzed, which assumes an exponential variation of resistivity through the oxide layer.

   - The native oxide of the SLM 316L stainless steel has slightly better barrier properties than that of its wrought counterpart.

   - The capacitance of the passive layer of the wrought sample was consistently higher than that of the SLM specimen (~ 1.8 times higher). Therefore, because the oxide film thickness was approximately the same for all the samples (as calculated by XPS), the dielectric constant of the oxide layer of the wrought material was higher than the dielectric constant of the oxide film of the SLM 316L sample (~ 1.8 times higher).

   - The conductivity of the native oxide layer of the wrought sample at the metal/oxide interface was around 3 orders of magnitude smaller than that of the SLM 316L specimen. Marked differences were observed in the conductivity profile of the oxide film of the wrought and SLM samples.

   The great differences found in the dielectric properties and conductivity profile of the oxide layer of the samples suggested the existence of structural differences between the passive films of the wrought and the SLM 316L SS.

Data availability
The raw/processed data required to reproduce these findings cannot be shared at this time as the data also forms part of an ongoing study.

Acknowledgement

References

1. A. J. Sedriks, Corrosion of stainless steels, 2nd edition,Wiley-Interscience, New York (1996).
2. J. R. Davis, ASM Specialty Handbook - Stainless Steels, ASM International (1994).
3. M.P. Ryan, D.E. Williams, R.J. Chater, B.M. Hutton, D.S. McPhail, Why stainless steel corrodes, Nature 415 (2002) 770–774.
4. D.G. Li, J.D. Wang, D.R. Chen, P. Liang, Molybdenum addition enhancing the corrosion behaviors of 316L stainless steel in the simulated cathodic environment of proton exchange membrane fuel cell, Int. J. Hydrog. Energy 40 (2015) 5947-5947.
5. A. Pardo, M.C. Merino, A.E. Coy, F. Viejo, R. Arrabal, E. Matykina, Effect of Mo and Mn additions on the corrosion behaviour of AISI 304 and 316 stainless steels in H_2SO_4, Corr. Sci. 50 (2008) 780-794.
6. A. Pardo, M.C. Merino, A.E. Coy, F. Viejo, R. Arrabal, E. Matykina, Pitting corrosion behaviour of austenitic stainless steels – combining effects of Mn and Mo additions, Corr. Sci. 50 (2008) 1796-1806.
7. K. Sugimoto, Y. Sawada, The role of alloyed Molybdenum in austenitic stainless steels in the inhibition of pitting in neutral halide solutions, Corrosion 32 (1976) 347-352.
8. S. Gorsse, C. Hutchinson, M. Goune, R. Banerjee, Additive manufacturing of metals : a brief review of the characteristic microstructures and properties of steels, Ti-6Al-4V and high-entropy alloys, Sci. Technol. Adv. Mater. 18 (2017) 584-610.
9. D.D. Gu, W. Meiners, K. Wissenbach, R. Poprawe, Laser additive manufacturing of metallic components: materials, processes and mechanisms, Int. Mater. Rev. 57 (2012) 133-164.
10. L.E. Murr, S.M. Gaytan, D.A. Ramirez, E. Martinez, J. Hernandez, K.N. Amato, P.W. Shindo, F.R. Medina, R.B. Wicker, Metal fabrication by additive manufacturing using laser and electron beam melting technologies, J. Mater. Sci. Technol. 28 (2012) 1-14.
11. L.E. Murr, E. Martinez, K.N. Amato, S.M. Gaytan, J. Hernandez, D.A. Ramirez, P.W. Shindo, F. Medina, R.B. Wicker, Fabrication of metal and alloy components by additive manufacturing: examples of 3D materials science, J. Mater. Res. Technol. 1 (2012) 42-54.
12. D. Herzog, V. Seyda, E. Wycisk, C. Emmelmann, Additive manufacturing of metals, Acta Mater. 117 (2016) 371-392.
13. W.J. Sames, F.A. List, S. Pannala, R.R. Dehoff, S.S. Babu, The metallurgy and processing science of metal additive manufacturing, Int. Mater. Rev. 61 (2016) 315-360.
14. K. Saeidi, X. Gao, F. Lofaj, L. Kvetkova, Z.J. Shen, Transformation of austenite to duplex austenite-ferrite assembly in annealed stainless steel 316L consolidated by laser melting, J. Alloys Compd. 633 (2015) 463-468.
15. K. Saeidi, X. Gao, Y. Zhong, Z.J. Shen, Hardened austenite steel with columnar sub-grain structure formed by laser melting, Mater. Sci. Eng. A 625 (2015) 221-229.
16. M. Zietala, T. Durejko, M. Polanski, I. Kunce, T. Plocinski, W. Zielinski, M. Lazinska, W.Stepniowski, T. Czujko, K.J. Kurzydlowski, Z. Bojar, The microstructure, mechanical properties and corrosion resistance of 316L stainless steel fabricated using laser engineered net shaping, Mater. Sci. Eng. A 677 (2016) 1-10.

17. F. Andreatta, A. Lanzutti, E. Vaglio, G. Totis, M. Sortino, L. Fedrizzi, Corrosion behaviour of 316L stainless steel manufactured by selective laser melting, Mater. Corr. (2019) 1-13.

18. M.J.K. Lodhi, K.M. Deen, M.C. Greenlee-Wacker, W. Haider, Additively manufactured 316L stainless steel with improved corrosion resistance and biological response for biomedical applications, Addit. Manuf. 27 (2019) 8-19.

19. M.J.K. Lodhi, K.M. Deen, W. Haider, Corrosion behavior of additively manufactured 316L stainless steel in acidic media, Materialia 2 (2018) 111-121.

20. J.R. Trelewicz, G.P. Halada, O.K. Donaldson, G. Manogharan, Microstructure and corrosion resistance of laser additively manufactured 316L stainless steel, J. Mater. 68 (2016) 850-859.

21. T. Kurzynowski, K. Gruber, W. Stopyra, B. Kuznicka, E. Chlebus, Correlation between process parameters, microstructure and properties of 316L stainless steel processed by selective laser melting, Mater. Sci. Eng. A 718 (2018) 64-73.

22. Y. Zhang, J. Zhang, Q. Yan, L. Zhang, M. Wang, B. Song, Y. Shi, Amorphous alloy strengthened stainless steel manufactured by selective laser melting: Enhanced strength and improved corrosion resistance, Scripta Materialia 148 (2018) 20-23.

23. Q. Chao, V. Cruz, S. Thomas, N. Birbilis, P. Collins, A. Taylor, P.D. Hodgson, D. Fabijanic, On the enhanced corrosion resistance of a selective laser melted austenitic stainless steel, Scripta Materialia 141 (2017) 94-98.

24. S.H. Sun, T. Ishimoto, K. Hagihara, Y. Tsutsumi, T. Hanawa, T. Nakano, Excellent mechanical and corrosion properties of austenitic stainless steel with a unique crystallographic lamellar microstructure via selective laser melting, Scripta Materialia 159 (2019) 89–93.

25. G. Sander, S. Thomas, V. Cruz, M. Jurg, N. Birbilis, X. Gao, M. Brameld, C.R. Hutchinson, On the corrosion and metastable pitting characteristics of 316L stainless steel produced by selective laser melting, J. Electrochem. Soc. 164 (2017) C250-C257.

26. Y. Sun, A. Moroz, K. Alrbaey, Sliding wear characteristics and corrosion behaviour of selective laser melted 316L stainless steel, J. Mater. Eng. Perform. 23 (2014) 518-526.

27. D. Kong, X. Ni, C. Dong, L. Zhang, C. Man, J. Yao, K. Xiao, X. Li, Heat treatment effect on the microstructure and corrosion behavior of 316L stainless steel fabricated by selective laser melting for proton exchange membrane fuel cells, Electrochimica Acta 276 (2018) 293-303.

28. P. Ganesh, R. Giri, R. Kaul, P.R. Sankar, P. Tiwari, A. Atulkar, R.K. Porwal, R.K. Dayal, L.M. Kukreja, Studies on pitting corrosion and sensitization in laser rapid manufactured specimens of type 316L stainless steel, Mater. Design 39 (2012) 509-521.

29. M.E. Orazem, I. Frateur, B. Tribollet, V. Vivier, S. Marcelin, N. Pebere, A.L. Bunge, E.A. White, D.P. Riemer, M. Musiani, Dielectric properties of materials showing constant-phase-element (CPE) impedance response, J. Electrochem. Soc. 160 (2013) C215-C225.

30. I. Frateur, Characterization of oxide films by electrochemical impedance, ECS Transactions 13 (2008) 115-128.

31. J. Evertsson, F. Bertram, F. Zhang, L. Rullik, L.R. Merte, M. Shipilin, M. Soldemo, S. Ahmadi, N. Vinogradov, F. Carlà, J. Weissenrieder, M. Göthelid, J. Pan, A. Mikkelsen, J.O. Nilsson, E. Lundgren, The thickness of native oxides on aluminum alloys and single crystals, Appl. Surf. Sci. 349 (2015) 826-832.

32. M.T. Woldemedhin, D. Raabe, A.W. Hassel, Characterization of thin anodic oxides of Ti–Nb alloys by electrochemical impedance spectroscopy, Electrochim. Acta 82 (2012) 324-332.

33. Y. Liu, Z. Wang, W. Ke, Study on influence of native oxide and corrosion products on atmospheric corrosion of pure Al, Corr. Sci. 80 (2014) 169-176.

34. O. Kerrec, D. Devilliers, H. Groult, M. Chemla, Dielectric properties of anodic oxide films on tantalum, Electrochim. Acta 40 (1995) 719-724.

35. C.M. Abreu, M.J. Cristóbal, R. Losada, X.R. Nóvoa, G. Pena, M.C. Pérez, Comparative study of passive films of different stainless steels developed on alkaline medium, Electrochim. Acta 49 (2004) 3049-3056.

36. J.B. Bessone, D.R. Salinas, C.E. Mayer, M. Ebert, W.J. Lorenz, An EIS study of aluminium barrier-type oxide films formed in different media, Electrochim. Acta 37 (1992) 2283-2290.

37. D. Wallinder, J. Pan, C. Leygraf, A. Deblanc-Bauer, EIS and XPS study of surface modification of 316L VM stainless steel after passivation, Corr. Sci. 41 (1999) 275-289.

38. M. Aronniemi, J. Sainio, J. Lahtinen, Chemical state quantification of iron and chromium oxides using XPS : the effect of the background substraction method, Surf. Sci. 578 (2005)108-123.

39. M.C. Biesinger, B.P. Payne, A.P. Grosvenor, L.W.M. Lau, A.R. Gerson, R.St.C. Smart, Resolving surface chemical states in XPS analysis of first row transition metals, oxides and hydroxides: Cr, Mn, Fe, Co and Ni, Appl. Surf. Sci. 257 (2011) 2717-2730.

40. K. Asami, K. Hashimoto, S. Shimodaira, XPS determination of compositions of alloy surfaces and surface oxides on mechanically polished iron-chromium alloys, Corr. Sci. 17 (1977) 713-723.

41. M. E. Orazem and B. Tribollet, *Electrochemical Impedance Spectroscopy*, Hoboken, NJ, USA: John Wiley & Sons Inc., 2008.

42. G.J. Brug, A.L.G. van den Eeden, M. Sluyters-Rehbach, J.H. Sluyters, The analysis of electrode impedances complicated by the presence of a constant phase element, J. Electroanal. Chem. 176 (1984) 275-295.

43. B. Hirschorn, M.E. Orazem, B. Tribollet, V. Vivier, I. Frateur, M. Musiani, Constant-phase-element behavior caused by resistivity distributions in films: Theory, J. Electrochem. Soc. 157 (2010) C452-C457.

44. B. Hirschorn, M.E. Orazem, B. Tribollet, V. Vivier, I. Frateur, M. Musiani, Constant-phase-element behavior caused by resistivity distributions in films: Aplications, J. Electrochem. Soc. 157 (2010) C458-C463.

45. L. Young, The interpretation of impedance measurements on oxide coated electrodes on niobium, Trans. Faraday Soc. 51 (1955) 1250-1260.

46. L. Young, Anodic Oxide Films, Academic, New York 1961.

47. Y.M. Chen, A.S. Nguyen, M.E. Orazem, B. Tribollet, N. Pebere, M. Musiani, V. Vivier, Identification of resistivity distributions in dielectric layers by measurement model analysis of impedance spectroscopy, Electrochimica Acta 219 (2016) 312-320.

48. Z. Feng, X. Cheng, C. Dong, Lin Xu, X. Li, Passivity of 316L stainless steel in borate buffer solution studied by Mott–Schottky analysis, atomic absorption spectrometry and X-ray photoelectron spectroscopy, Corr. Sci. 52 (2010) 3646–3653.

49. I. Betova, M. Bojinov, P. Kinnunen, K. Lundgren, T. Saario, Influence of Zn on the oxide layer on AISI 316L(NG) stainless steel in simulated pressurised water reactor coolant, Electrochimica Acta 54 (2009) 1056–1069.

50. I. Nicic, D.D. Macdonald, The passivity of Type 316L stainless steel in borate buffer solution, J. Nuclear Mater. 379 (2008) 54–58.

51. J.J. Kim, Y.M. Young, Study on the passive film of type 316 stainless steel, Int. J. Electrochem. Sci. 8 (2013) 11847-11859.

52. G. Gomila, G. Gramse, L. Fumagalli, Finite-size effects and analytical modeling of electrostatic force microscopy applied to dielectric films, Nanotechnology 25 (2014) 255702.

53. R.I. Revilla, The jump-into-contact effect in biased AFM probes on dielectric films and its application to quantify the dielectric permittivity of thin layers, Nanotechnology 27 (2016) 265705.

54. R.I. Revilla, X.J. Li, Y.L. Yang, C. Wang, Comparative method to quantify dielectric constant at nanoscale using atomic force microscopy, J. Phys. Chem. C 118 (2014) 5556-5562.

55. R.I. Revilla, Y.L. Yang, C. Wang, Local surface charge dissipation studied using force spectroscopy method of atomic force microscopy, Surf. Interface Anal. 47 (2015) 657-662.
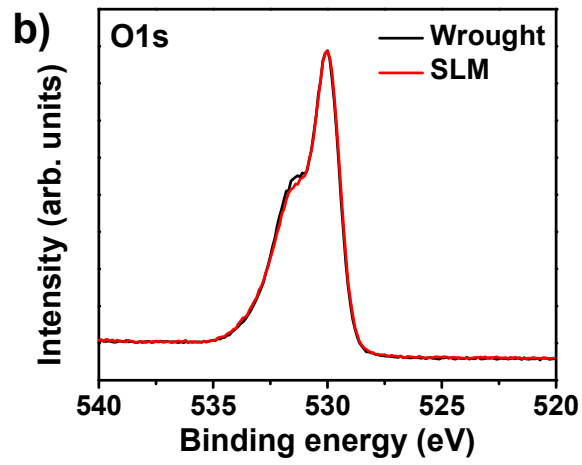
Figures
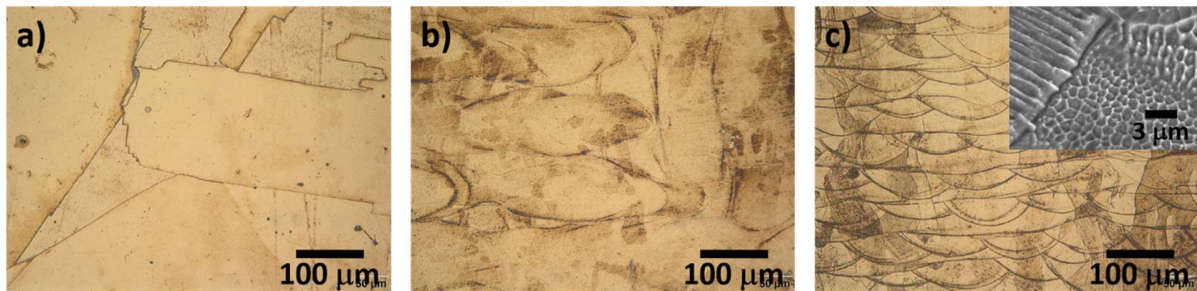
Figure 1. Optical images of the etched surface of the wrought (a), SLM-XY (b), and SLM-XZ 316L specimens. The inset in (c) represents a higher magnification secondary electron microscopy image of the SLM samples.
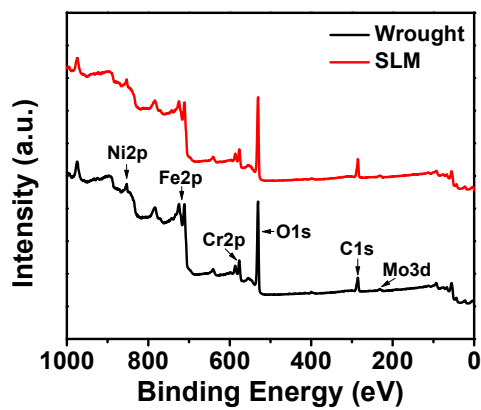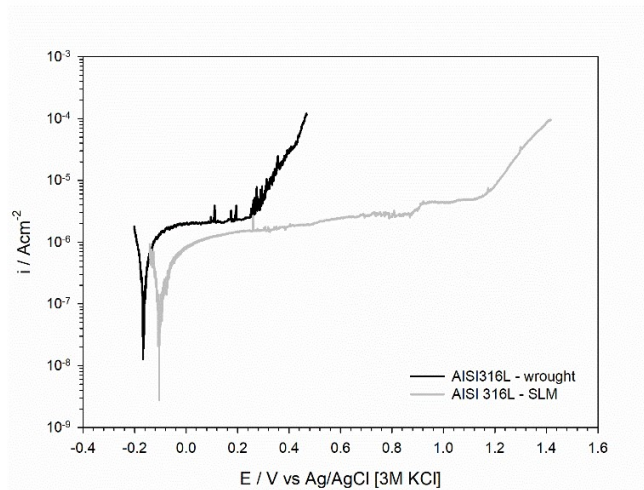

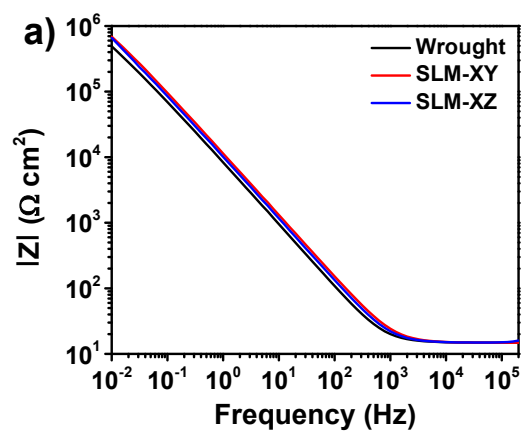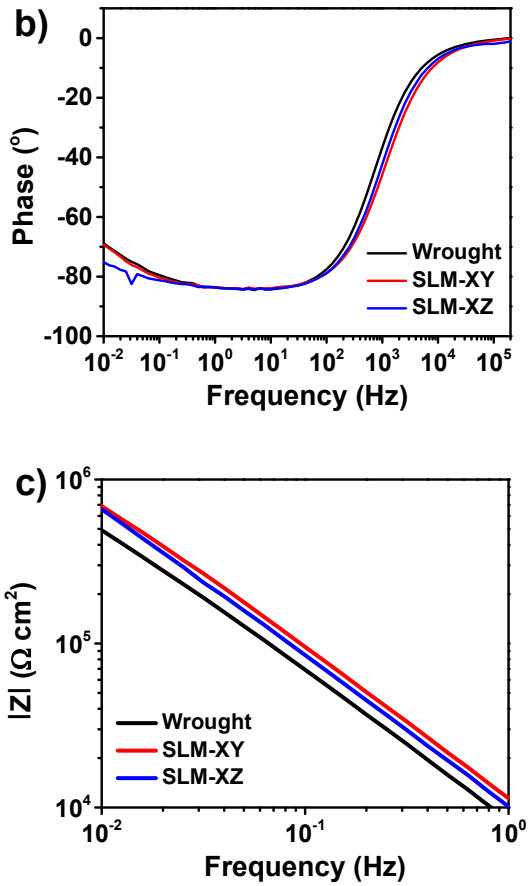**Figure 2.** XPS survey spectra of the wrought and SLM 316L SS samples.
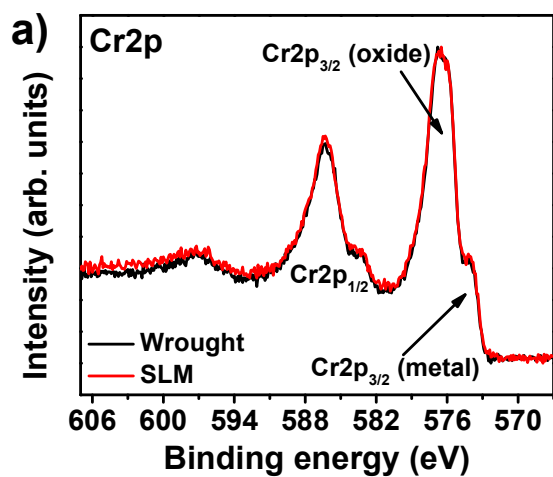
Figure 3. High-resolution XPS spectra of the (a) Cr2p and (b) O1s region for the wrought and SLM 316L SS samples.


Figure 4. Potentiodynamic polarization curves of wrought and SLM 316L SS specimens in 3.5 wt% NaCl.

Figure 5. Representative Bode plots from the EIS measurements conducted in 3.5 % NaCl solution after 1 h of immersion. (a) Impedance modulus and (b) Phase angle. (c) Zoom of the impedance plot in the frequency range from 1 to 10^{-2} Hz. The data is represented with lines instead of dots in order to better see the difference between the SLM sample and the wrought material.
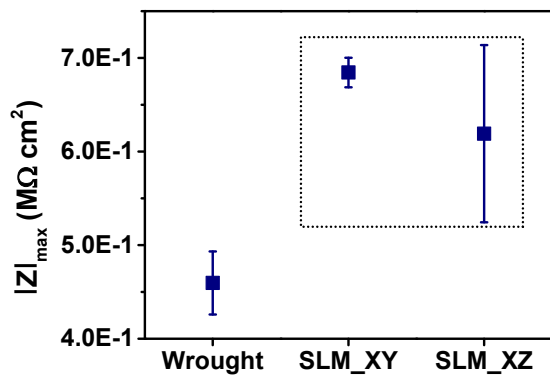
**Figure 6.** Average impedance measured at the lowest frequency (10^{-2} Hz).
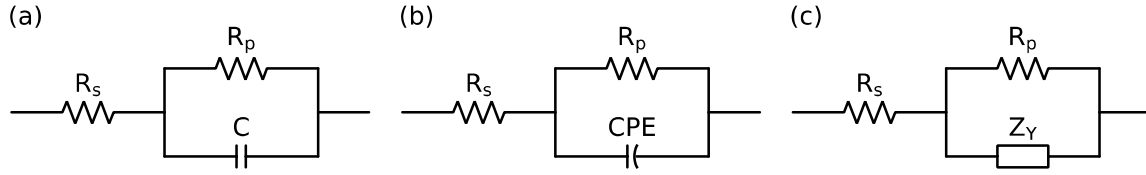
Figure 7. Equivalent electrical circuits used to model impedance data in the case of native oxide layers on the surface of metals and alloys using a capacitor (a), a constant phase element (CPE) (b), and a Young impedance (Z_Y) (c). Rs represents the electrolyte resistance and Rp a parallel resistance.


$$y = 6.66E8e^{-21.47x}$$
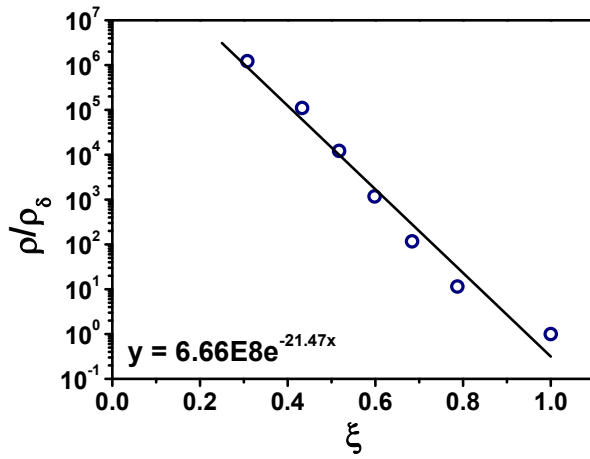
Figure 8. Dimensionless resistivity (ρ/ρ_δ) as a function of dimensionless position (ξ). ρ and ξ are the resistivity and the relative position respectively calculated from the parameters obtained from the Voigt model [47]. ρ_δ is the boundary value of resistivity at the film-electrolyte interface. The solid line represents the linear fitting of the data in a semi-logarithmic scale. This curve was constructed with EIS response obtained in the SLM_XY specimen as an example. The same behavior was obtained for all the data measured in all the specimens.
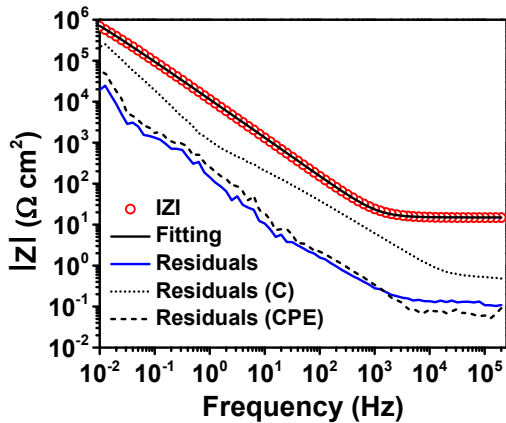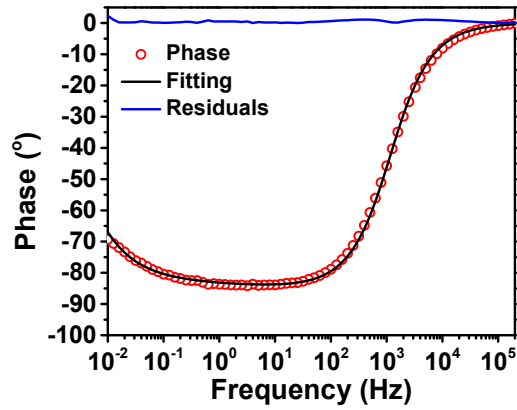
Figure 9. Example of a fitted electrochemical impedance data using a Young element (Figure 7c). The EIS signal of the SLM-XY specimen was taken as an example. The blue line represents the residuals obtained from the fitting using the Young model while the discontinuous lines are the residuals using a capacitor and a CPE for comparison.
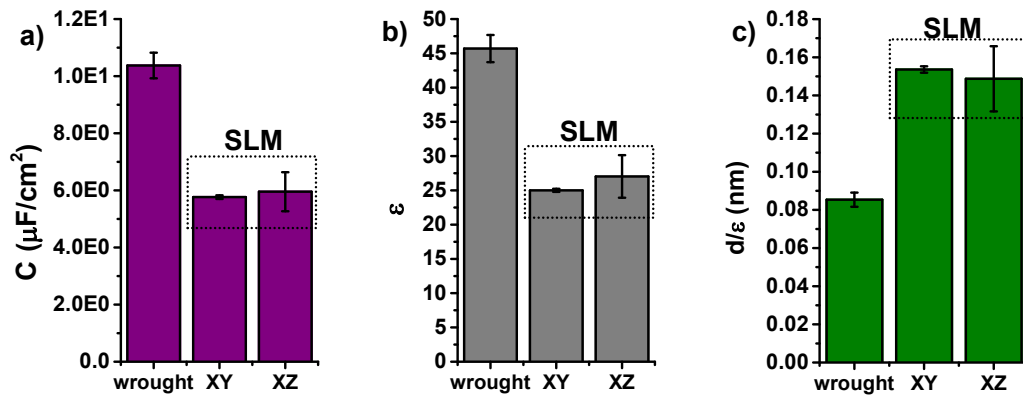

Figure 10. (a) Average values of the capacitance of the native oxide film calculated using the Young model. (b) Dielectric constant of the passive layer calculated using the average values of capacitance. (c) Effective dielectric thickness of the oxide layer (d/ε).
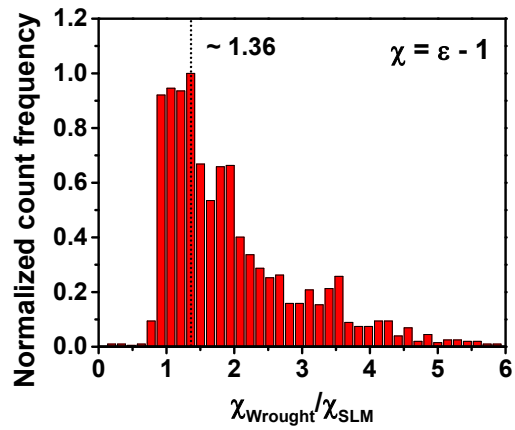
Figure 11. Values of the ratio between the dielectric susceptibilities of the samples obtained using the approach described in ref. [54].
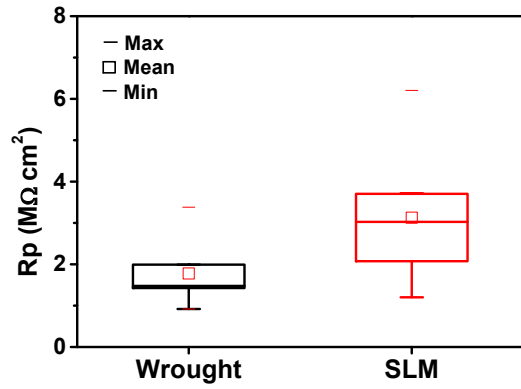
Figure 12. Box plots of the parallel resistance obtained using the Young model for the wrought and the SLM 316L specimens.
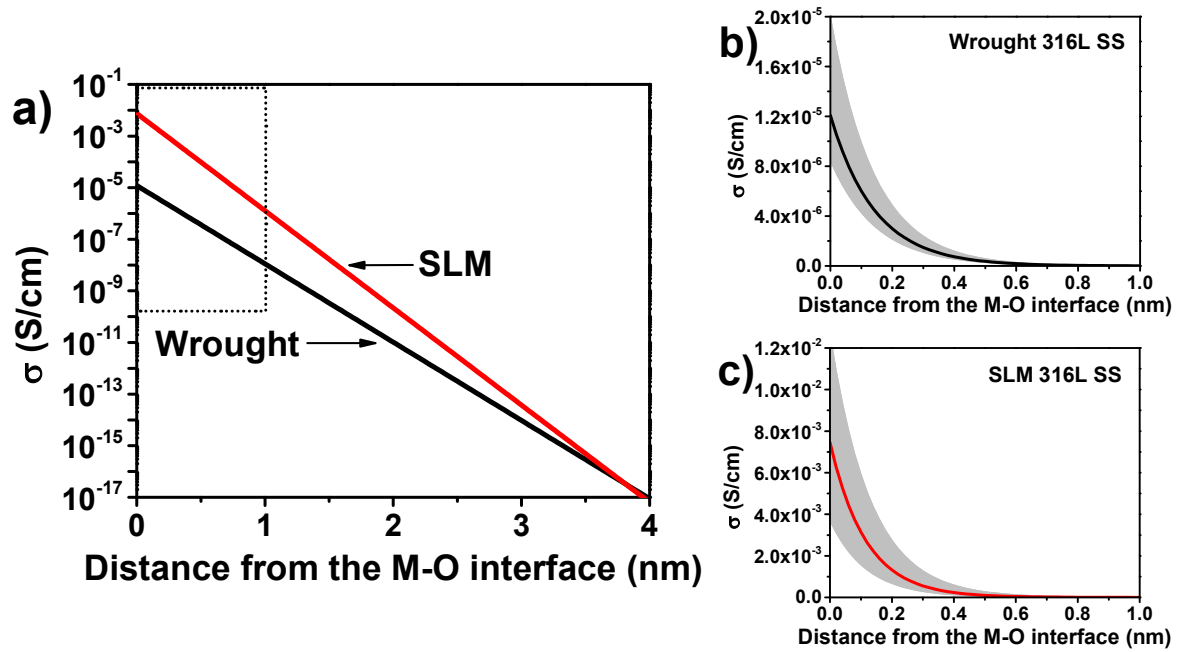
Figure 13. (a) Mean conductivity profile for the wrought and the SLM 316L specimens in a semi-logarithmic scale calculated from the regressed values of the characteristic length (δ) and the conductivity at the metal/oxide interface (σ_0) obtained from the fitting using the Young model. (b) and (c) represent respectively the conductivity profiles of the oxide films on the surface of the wrought and the SLM 316L samples for the first nm. The grey area is delimited by the highest and the lowest curve obtained.
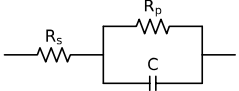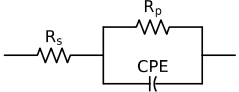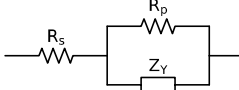
Tables

Table 1. Chemical composition (wt%) of the 316L stainless steel powder.

Cr	Ni	Mo	Mn	Si	S	C	*p*	Fe
17.7	12.6	2.4	1.1	0.6	0.004	0.025	<0.045	Balance

Table 2. Average values and relative standard deviation of the different parameters obtained per sample type from the fitting of the data using different EECs. Rs and Rp have units of Ω; C and C_Y have units of F; Q has units of $F/s^{(1-\alpha)}$; and τ is in s. p and α are dimensionless quantities.

		Wrought	AM-XY	AM-XZ
	Rs	19.31 (3.74%)	19.07 (1.7%)	18.79 (2.84%)
	C	1.48E-05 (3.56%)	1E-05 (2.52%)	1.12E-05 (5.78%)
	Rp	1.02E+06 (22.2%)	1.63E+06 (3.96%)	1.23E+06 (57.2%)
	Rs	18.65 (2.08%)	18.73 (1.08%)	18.62 (2.38%)
	Q	1.85E-05 (4.14%)	1.28E-05 (4.89%)	1.57E-05 (1.12%)
	α	0.9292 (0.81%)	0.9282 (0.65%)	0.9202 (1.7%)
	Rp	1.77E+06 (41.3%)	2.9E+06 (12.5%)	2.14E+06 (61.6%)
	Rs	18.77 (1.97%)	19.06 (0.05%)	18.94 (1.12%)
	C_Y	8.15E-6 (4.34%)	4.53E-6 (1.1%)	4.68E-6 (11.5%)
	p	0.0367 (2.42%)	0.0305 (0.56%)	0.0312 (6.53%)
	τ	2.91E-7 (55.1%)	5.92E-10 (0.72%)	2.55E-10 (29.6%)
	Rp	2.26E+6 (48.1%)	4.13E+6 (14%)	3.89E+6 (66.3%)

Appendix: Table summarizing the most relevant studies carried out to date concerning the corrosion behavior of additive manufactured 316L stainless steel compared with conventionally manufactured specimens. In the table is specified the additive manufactured process used, the electrolyte in which the corrosion test was performed, and the main conclusions drawn from the corrosion tests (for instance, the corrosion resistance of the AM specimen relative to the conventional sample).

Ref.	AM process used	Test electrolyte	Main conclusions drawn	
			Corrosion resistance compared to ref. sample	Other relevant conclusions
[22]	SLM	3.5 wt% NaCl	SLM > As-cast	
[23]	SLM	0.6M NaCl	SLM > Wrought	High solidification rates inherent to AM avoided MnS formation and an associated Cr-depletion zone.
[24]	SLM	0.9 wt% NaCl	SLM > Wrought	
[25]	SLM	0.1M NaCl	SLM > Wrought	E_{corr}, I_{corr}, and E_{pit} values of the AM specimens did not vary significantly with the specimen porosities.
[17]	SLM	3.5 wt% NaCl	SLM > Wrought	The thickness and the composition of the oxide film on SLM and wrought specimens are very similar.
[18]	SLM	Human serum, phosphate buffer saline (PBS), and 0.9M NaCl	SLM > Wrought	EIS suggest better barrier properties for the AM specimen compared to the wrought sample.
[19]	SLM	Deionized water with and without Cl^- (400 ppm) at pH 1, 2, and 3	SLM > Wrought	EIS suggest better barrier properties for the AM specimen compared to the wrought sample.
[26]	SLM	0.9 wt% NaCl	Wrought > SLM	The pre-existing pores in SLM samples are preferentially attacked during corrosion, leading to increased metal dissolution, breakdown of passivity and pitting corrosion at low anodic potentials.
[27]	SLM	0.5 M H_2SO_4 with 50 ppm Cl^- and 2 ppm F^-	Wrought > SLM	
[28]	LRN	3.5 wt% NaCl	Wrought > LRN	

[16]	LENS	0.9 wt% NaCl	Wrought > LENS	LENS 316L exhibited lower values of I_{corr} than the wrought. However, the LENS samples presented lower values of $E_{breakdown}$.
[20]	PBF-L	0.1M HCl	Wrought > PBF-L	